

# Integrated multimodal microscopy, time-resolved fluorescence, and optical-trap rheometry: toward single molecule mechanobiology

**Ramachandra R. Gullapalli\***

**Tristan Tabouillot\***

The Pennsylvania State University  
Department of Bioengineering  
205 Hallowell Building  
University Park, Pennsylvania 16802

**Rishi Mathura**

The City College of New York  
Department of Biomedical Engineering  
13th Street and Convent Avenue  
New York, New York 10031

**Jhanvi H. Dangaria**

**Peter J. Butler**

The Pennsylvania State University  
Department of Bioengineering  
205 Hallowell Building  
University Park, Pennsylvania 16802

**Abstract.** Cells respond to forces through coordinated biochemical signaling cascades that originate from changes in single-molecule structure and dynamics and proceed to large-scale changes in cellular morphology and protein expression. To enable experiments that determine the molecular basis of mechanotransduction over these large time and length scales, we construct a confocal molecular dynamics microscope (CMDM). This system integrates total-internal-reflection fluorescence (TIRF), epifluorescence, differential interference contrast (DIC), and 3-D deconvolution imaging modalities with time-correlated single-photon counting (TCSPC) instrumentation and an optical trap. Some of the structures hypothesized to be involved in mechanotransduction are the glycocalyx, plasma membrane, actin cytoskeleton, focal adhesions, and cell-cell junctions. Through analysis of fluorescence fluctuations, single-molecule spectroscopic measurements [e.g., fluorescence correlation spectroscopy (FCS) and time-resolved fluorescence] can be correlated with these subcellular structures in adherent endothelial cells subjected to well-defined forces. We describe the construction of our multimodal microscope in detail and the calibrations necessary to define molecular dynamics in cell and model membranes. Finally, we discuss the potential applications of the system and its implications for the field of mechanotransduction. © 2007 Society of Photo-Optical Instrumentation Engineers. [DOI: 10.1117/1.2673245]

**Keywords:** endothelial cell; membrane; total internal reflection fluorescence; mechanotransduction; fluorescence correlation spectroscopy; time-correlated single-photon counting.

Paper 06160R received Jun. 15, 2006; revised manuscript received Sep. 7, 2006; accepted for publication Sep. 23, 2006; published online Mar. 2, 2007.

## 1 Introduction

Biological cells convert forces to intracellular biochemical signaling cascades by mechanotransduction, a process that is responsible for diverse physiological phenomena including bone and vascular wall remodeling, vascular caliber control, and embryonic development.<sup>1</sup> In contrast, atherosclerosis, sensory dysfunction in diabetes mellitus, and hair cell damage in the inner ear leading to vertigo are examples of cellular mechanical regulatory processes gone awry.<sup>2</sup> Physiological forces arise from blood-flow-induced shear stresses, hydrostatic pressure, extracellular matrix deformations, intracellular contractions, and osmotic swelling. The length scale of these forces spans single molecules, cellular organelles, cells, tissues, organs, and physiological systems; the time scales span nanoseconds to days.<sup>3</sup>

The essential ingredients of a comprehensive understanding of mechanotransduction are a well-defined force, cellular mechanical properties, and a physiological readout directly related to the force. Well-defined forces arise from fluid flow,<sup>4</sup> atomic force microscopes,<sup>5,6</sup> optical traps,<sup>7</sup> and magnetic beads.<sup>8</sup> Cellular deformations of these forces can be modeled using continuum mechanics<sup>8-10</sup> or ultrastructural characterization of load-bearing structures.<sup>11-13</sup> Examples of readouts of force-induced physiological responses include calcium signaling,<sup>14</sup> ion channel activity,<sup>15</sup> phosphorylation of proteins,<sup>16</sup> and transcription<sup>17</sup> of new RNA. A major challenge in mechanotransduction is to differentiate mechanosensors (cellular structures that are perturbed by physical forces), mechanotransducers (molecules that undergo biochemical changes in response to force and initiate signaling cascades), and mechanobiology (the resultant changes in cellular structure and function).

Analysis of single molecules in cells subjected to force can provide the link between force and mechanotransduction. Major technical and computational advances in analysis of fluo-

\*These authors contributed equally.

Address all correspondence to: Peter J. Butler, PhD, The Pennsylvania State University, Department of Bioengineering, 228 Hallowell Building, University Park, PA 16802; Tel: (814) 865-8086; Fax: (814) 863-0490; Email: pbutler@psu.edu

rescence fluctuations provide new methods to assess single-molecule dynamics in model and cellular systems.<sup>18,19</sup> For example, time-correlated single photon counting (TCSPC) instrumentation is available on a single compact PCI, (peripheral component interconnect) card that, when integrated with pulsed and continuous wave lasers, can be used to assess nanosecond- to second-scale dynamics of single fluorescent molecules. Analysis methods including fluorescence correlation spectroscopy (FCS) and fluorescence lifetime can then be used to gain information on diffusion, conformational changes, aggregation, chemical kinetics, and other important biomolecular phenomena.<sup>18,19</sup>

In this paper, we describe the construction and calibration of a confocal molecular dynamics microscope (CMDM) capable of (1) applying cell-scale forces using micropipette aspiration, optical traps, and fluid flow; (2) assessing cellular mechanical properties using optical trap and particle-tracking microrheology; and (3) correlating molecular-scale physiological readouts from TCSPC with cellular structures imaged with multimodal microscopy. The intended application of this system is to assess force-induced changes in dynamics of molecules occurring on a time scale of nanoseconds, while addressing long-term adaptive responses of cells on the order of hours. It is anticipated that these new tools will enable a comprehensive analysis of cellular mechanobiology and lead to major clinical advances in treating or preventing diseases such as atherosclerosis, which have their origins in mechanotransduction.<sup>2</sup>

We begin with a background on the theory of FCS, optical traps, and multimodal microscopy. We then describe the detailed construction and implementation of the CMDM. Finally, we present results of calibration experiments in which molecular diffusion is analyzed in solutions and in model and cellular membranes.

## 2 Background

### 2.1 FCS

The detection of single molecules in femtoliter volumes was made possible by the development of confocal optics, high-sensitivity detectors, and robust fluorophores.<sup>20</sup> Probe molecules move into and out of a confocal volume yielding fluorescence fluctuations (Fig. 1). Autocorrelation analysis of these fluctuations can provide diffusion coefficients and other single-molecule information.<sup>21,22</sup>

In the following analysis, we consider the relationship between autocorrelation of fluorescence fluctuations and molecular diffusion. We begin with the Stokes-Einstein relationship for the diffusion coefficient  $D$  of a sphere with a hydrodynamics radius  $R$  in a solvent of viscosity  $\eta$ :

$$D = \frac{k_B T}{6\pi\eta R}, \quad (1)$$

where  $k_B$  is the Boltzmann constant, and  $T$  is absolute temperature. We define a 2-D characteristic molecular diffusion transit time  $\tau_D$  across a small area of radius  $r$  such that

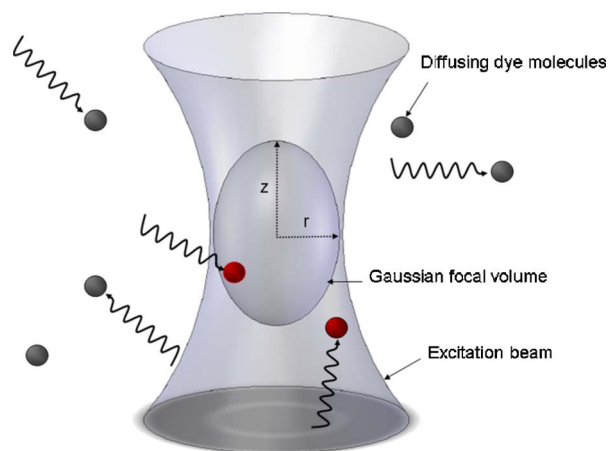


**Fig. 1** Confocal volume for FCS. The radial dimension  $r$  of the confocal volume is close to the diffraction limit of the objective and is determined by keeping the  $(r/z)$  parameter constant ( $<10$ ) in Eq. (6) when fitting the autocorrelation curve from R6G molecules in water. The radius thus obtained from experiment is  $326 \pm 10$  nm. Fluorescent molecules are excited by the entire laser beam and fluorescence emission is only collected in the confocal volume. When particles move into and out of the confocal volume in the  $x$ ,  $y$ , and  $z$  directions, 3-D diffusion is considered. When particles only move in the  $x$ - $y$  plane, 2-D diffusion is considered.

$$r^2 = 4D\tau_D. \quad (2)$$

Under conditions of equilibrium, the fluorescence fluctuates around an average value  $\langle F \rangle$ , due to diffusion. The intensity of these fluctuations  $\delta F(t)$  can be autocorrelated to obtain the autocorrelation function  $G(\tau)$  given by

$$G(\tau) = \frac{\langle \delta F(t + \tau) \delta F(t) \rangle}{\langle F(t) \rangle^2}, \quad (3)$$

where  $t$  (time) and  $\tau$  (lag time) vary over all times of the data collection period. The fluorescence fluctuations are related to the instantaneous change in concentration  $\delta C(r, t)$  in the observation volume. To relate the autocorrelation function to diffusion, we use the diffusion equation:

$$D\nabla^2 \delta C(r, t) = \frac{\partial \delta C(r, t)}{\partial t}, \quad (4)$$

and the relationship between fluorescence fluctuations and concentration of the fluorescent molecules in the confocally defined optical probe volume:

$$\delta F(t) = K \int_{\text{volume}} \delta C(r, t) I(r) \theta(r), \quad (5)$$

where  $I(r)$  is the excitation intensity profile,  $\theta(r)$  is the collection efficiency profile, and  $K$  is a proportionality constant. The confocal probe volume is created by placing a small aperture (pinhole or fiber optic) in an image plane that is conjugate to the focus of a high-numerical-aperture, infinity-corrected objective. The laser beam has a Gaussian intensity profile that fills the back aperture of the objective, leading to a Gaussian illumination profile  $I(r)$  such that  $I(r) = I_0 \exp(-r^2/z^2)$ , where  $r$  and  $z$  are the probe volume ra-

dus and half-height, respectively, and are defined as the point where the intensity falls off to  $1/e^2$  of the maximum (center) intensity (Fig. 1). A single constant factor known as the structure factor  $\omega$  is defined as the ratio of  $z/r$ . The autocorrelation obtained from the experiment and its relation to the theoretical Gaussian confocal volume and the characteristic diffusion time is<sup>21-23</sup>

$$G(\tau) = \frac{1}{N} \left[ \frac{1}{1 + (\tau/\tau_D)} \right] \left[ \frac{1}{1 + (1/\omega)^2 (\tau/\tau_D)} \right]^{1/2}, \quad (6)$$

where  $N$  is the average number of diffusing fluorophores in the confocal volume. The number of fluorescent molecules present in the sample volume is the inverse of the term  $G(0)$ .

The relationship between the autocorrelation function and diffusion on 2-D structures (e.g., plasma membrane) is given by

$$G(\tau) = \frac{1}{N} \left[ \frac{1}{1 + (\tau/\tau_D)} \right]. \quad (7)$$

This measurement in two dimensions can be extended to include multicomponent diffusion of multiple noninteracting species of fluorescent molecules, according to the equation

$$G(\tau) = \sum_{i=1}^n b_i \left[ \frac{1}{1 + (\tau/\tau_{Di})} \right], \quad (8)$$

where  $b_i$  is the relative proportion of the noninteracting diffusing molecules.

In the case of 2-D anomalous diffusion (e.g., in a cellular membrane), the time dependence of the mean square displacements is not linear but of the form  $\langle \Delta r^2 \rangle = \Gamma \tau^\alpha$ , and the autocorrelation is given by<sup>24</sup>

$$G(\tau) = \frac{1}{N} \frac{1}{1 + \Gamma \tau^\alpha / r^2}, \quad (9)$$

where  $\Gamma$  is the transport coefficient, and  $\alpha$  is the temporal exponent with values between zero and one. For a more comprehensive description of FCS including analysis of other sources of fluorescence fluctuations and detailed derivations of the equations presented here, see an excellent book by Zander et al.<sup>23</sup>

## 2.2 Fluorescence Lifetime

Time-resolved fluorescence lifetime spectroscopy enables analysis of subtle changes in photophysics of fluorescent molecules.<sup>25</sup> When a fluorescent molecule is excited to a higher energy state using a picosecond pulse of laser light, it remains in the excited state for a finite time before it decays to the ground-level energy state. Using a high-frequency pulsed laser, histograms of photon emission times relative to excitation times can be generated and fit with a negative exponential (or multiple exponentials) with a characteristic decay time (or lifetime)  $\tau$  (different from the characteristic diffusion time  $\tau_D$  of FCS). Fluorescence lifetime depends on local molecular microenvironmental factors including ionic strength, hydration, oxygen concentration, binding to macromolecules, and the proximity to other molecules that can deplete the excited state by resonance energy transfer.<sup>25</sup> The fluorescence lifetime

and quantum yield are related to intrinsic photophysical characteristics of a fluorescent molecule such as radiative and nonradiative decay mechanisms. The fluorescence quantum yield  $Q$  is the ratio of the number of photons emitted to the number of photons absorbed, according to

$$Q = \frac{k_r}{k_r + k_{nr}}, \quad (10)$$

where  $k_r$  and  $k_{nr}$  are the radiative and nonradiative decay rates of the molecule, respectively. Fluorescence lifetime is given by

$$\tau = \frac{1}{k_r + k_{nr}}. \quad (11)$$

The value for  $k_{nr}$  depends on the mode of the nonradiative decay, such as collisional quenching, hydration, and vibrational relaxation. Thus, any alteration of  $k_{nr}$  also leads to a detectable change in the value of the fluorescence lifetime.

The value for fluorescence lifetime is obtained by an iterative reconvolution of an instrument response function (IRF) with the fluorescence intensity using an assumed decay law, which can be approximated by a sum of exponentials:<sup>25</sup>

$$I(t) = \sum_i \alpha_i \exp(-t/\tau_i), \quad (12)$$

where  $\alpha_i$  is the fraction of molecules with lifetime  $\tau_i$ , normalized to unity. Fluorescence lifetimes are independent of fluorescence probe concentrations and can provide information not obtainable from intensity variations alone. When polarized light is used to excite a molecule whose excitation dipole is oriented parallel to the polarization of the pulse, it is possible to separate the parallel and perpendicular components of the emitted fluorescence signal and to extract rotational diffusion constants.<sup>25</sup>

## 2.3 Optical Trap

Optical traps apply piconewton-level forces to small beads or organelles, using momentum transfer from focused laser light. Although the ability of light to apply forces to matter was discovered by 1873 by Maxwell, it is only in the last two decades that laser and optics developments permitted application of optical trapping forces to cells and molecules.<sup>26,27</sup> Briefly, the energy carried as momentum by a traveling photon is translated into a net force on an object hit by that photon. The integrated photonic force on a particle in a Gaussian laser beam is given by<sup>28,29</sup>

$$\begin{aligned} \mathbf{F} &= -\alpha \frac{n_1 V}{c R^2} \left( \frac{n_2^2 - n_1^2}{n_2^2 + 2n_1^2} \right) I_0 \exp(-r^2/R^2) r \hat{r} \\ &\equiv -k_0 r \exp(-r^2/R^2), \end{aligned} \quad (13)$$

where  $\alpha$  is a geometrical factor of order one;  $n_1$  and  $n_2$  are the refractive indices of the surrounding medium and the particle, respectively;  $V$  is the volume of the bead;  $c$  is the speed of light in a vacuum;  $I_0$  is the intensity of the incident light;  $r$  is the distance between the centers of the bead and laser beam;  $\hat{r}$  is a unit vector; and  $R$  is the laser beam  $1/e^2$  radius. In practice, when  $r \ll R$ , the trap acts as a linear spring for small

displacements with a spring constant  $k_{0r}$  determined by equating the variance of 1-D displacements  $\langle(x-x_0)^2\rangle$  with the thermal fluctuations according to the equipartition theorem:

$$1/2k_{0r}\langle(x-x_0)^2\rangle = 1/2k_B T, \quad (14)$$

where  $x_0$  is the mean value of  $x$ ,  $k_B$  is the Boltzmann constant ( $1.38 \times 10^{-23}$  J/K),  $T$  is absolute temperature, and  $\langle \rangle$  refers to the time average. Alternatively, the trap strength can be measured by quantifying the displacement  $x$  of the bead due<sup>30</sup> to applied force  $F$  (e.g., from fluid flow) (i.e.,  $F = k_{0r}x$ ).

### 2.4 Multimodal Microscopy

To correlate molecular-scale events with cellular structures and their locations, we have integrated TCSPC and an optical trap into a multimodal microscope consisting of differential interference contrast (DIC), total internal reflection fluorescence (TIRF), and epifluorescence microscopy followed by deconvolution using AutoDeblur software (Autoquant, Albany, New York). A 3-D piezoelectric stage provides high-resolution positioning, such that molecular-scale analysis can be associated with subcellular regions of live adherent cells. Much of this hardware is commercially available, making these techniques accessible to researchers in biology and mechanobiology. The engineering challenge is to integrate these modalities on a single platform. In response to this challenge, microscope manufacturers have developed microscopes with multiple input and output ports and increased infinity space for the introduction of custom optics. To make this setup accessible to other researchers, we list all the component parts in Table 1. For detailed description of our multimodal microscopy setup the reader is referred to Ferko et al.<sup>10,31</sup>

## 3 Instrumentation and Setup

In this section we describe the details of the microscope and associated optics. All parts, part numbers, and manufacturers are listed in Table 1.

### 3.1 Microscope, Optics, and Camera

The CMDM is based on an Olympus IX71 and associated optics firmly secured to a vibration table. In the diascopic light path, a 100-W halogen light provides brightfield illumination for phase contrast and DIC microscopy. Our DIC setup employs a high-NA objective (LUMPlanFl 60 $\times$ /0.9 NA, WD 0.9 mm) as a condenser to increase contrast over traditional condenser designs. We use a water-immersion objective (UPLAPO 60 $\times$ /1.2 NA, WD 0.25 mm) or an oil-immersion objective (PLAPO 60 $\times$ /1.45 NA, TIRFM-2, WD 0.15 mm) for DIC, FCS, fluorescence lifetime measurements, and TIRF (oil only).

For TIRF, laser light is fiber-coupled to the TIRF illuminator on one end of the epiport and is focused off-center on the back aperture of the objective. Due to the high NA (1.45) of the objective, the incoming light is transmitted to the glass coverslip at an angle greater than the critical angle and is internally reflected there, resulting in an evanescent wave of light that decays exponentially with distance away from the coverslip. The fluorescent molecules at this interface within a distance of 200 nm from the top of the coverslip are selec-

tively excited. The angle of incidence of the laser beam at the interface is controlled by a micrometer on the TIRF illuminator attachment.

A CCD camera is attached to the left side port of the microscope. The camera exhibits high resolution and sensitivity due to the small CCD sensor element size (1376 $\times$ 1040 pixels; 6.45- $\times$ 6.45- $\mu\text{m}^2$  pixel size), high quantum efficiency (65%) in the visible range, and a two-stage Peltier cooling system (capable of attaining a temperature of  $-11^\circ\text{C}$ ). The cooling fan is placed remotely and connected to the camera by flexible plastic tubing to minimize transmission of vibrations from the fan to the microscope. The camera was modified with a fast shutter to enable the collection of two successive images with an interval of 500 ns.

### 3.2 Laser Sources

A cw krypton-argon-ion laser with stable TEM<sub>00</sub> mode laser light is used for both fluorescence correlation spectroscopy and TIRF illumination. The laser is air cooled and is placed away from the main table to reduce the propagation of the vibrations from the cooling fan to the microscope. The laser contains a prism-based micrometer adjustment to deliver wavelengths of 476, 483, 488, 496, 514, 520, 530, 568, 647, and 676 nm. A fiber coupling system has four adjustable screws to align the fiber with the laser. Once one fiber is aligned properly, multiple fibers can be used interchangeably with minimal realignment. An additional red, pulsed-diode laser ( $\lambda=650$  nm) is used for time-resolved fluorescence lifetime and FCS experiments in the far red excitation wavelength range. The average power of the diode laser is 100  $\mu\text{W}$  to 2 mW, with a repetition rate of 50 MHz and a pulse width of  $\sim 90$  ps. For lifetime measurements on dyes in the green excitation wavelength range, we use a water-cooled 80 MHz, 5.4 ps, 75 mW, pulsed solid state laser ( $\lambda=532$  nm, High-Q Laser, Hohenems, Austria).

### 3.3 3-D Piezostage and Nanometer-Scale Positioning

For high-precision and high-resolution 3-D positioning, we employ a piezoelectric microscope stage. The stage consists of a manual microstage and a three-axis piezo nanostage with 100  $\mu\text{m}$  of travel in each of three orthogonal directions. The nanostage can carry a load of up to 0.5 kg. Custom LabView code controls the movement of the nanostage and coordinates 3-D positioning of the focused laser beam with images from the camera.

### 3.4 TCSPC and Single-Molecule Fluorescence Spectroscopy

Fluorescence spectroscopy optics are connected to the right side port of the microscope (Fig. 2). The laser light exits the fiber, is expanded and collimated, reflects off the dichroic mirrors, and travels through the side port to the objective, which defines the probe volume and collects emitted fluorescence. The beam diameter is matched to the objective back aperture (7.2 mm) to ensure a Gaussian excitation profile and full use of the objective NA. Alternative beam parameters are discussed in Hess and Webb.<sup>32</sup> A laser power of 90  $\mu\text{W}$  measured at the objective back aperture ensures a good signal-to-noise ratio (SNR) without significant photobleaching or triplet state formation. Elimination of stray nonfluorescent light is

**Table 1** Components used in construction of the CMDM. The CMDM is comprised of modules for single molecule spectroscopy, multimodal microscopy, and an optical trap.

Components	Part Number and Supplier	Description
Microscope	IX-71 (Olympus, Tokyo, Japan)	Inverted microscope with left (camera), right (single-molecule fluorescence system) and back (epifluorescence and TIRFM) ports
Lasers	35-KAP-431-220 (Melles Griot, Carlsbad, California, USA)	CW Argon/Krypton-ion laser with 476 to 676-nm excitation; output power 4 to 20 mW
	PicoTRAIN (High-Q Laser, Hohenems, Austria)	water-cooled 532-nm, 80-MHz, 5.4-ps pulsed YAG laser; output power ~75 mW
	BHL-150 (Becker & Hickl, Berlin, Germany)	650-nm diode laser pulsed at 50 MHz; output power 0.1 to 2 mW
Optical fibers	Kineflex-P-3-S-488/568/647-0.65-FCP (Point-Source, Southampton, United Kingdom)	Polarization-maintaining single-mode optical fiber for 488, 514, and 647-nm light
	M14L01 (Thorlabs, Newton, New Jersey)	50- $\mu$ m-diam 0.22 numerical aperture (NA) optical fiber used as confocal pinhole
Microscope objectives	LUMPlanFI (Olympus, Tokyo, Japan)	60 $\times$ water-immersion objective 0.9 NA, used as condenser for DIC
	UPLAPO60XW (Olympus, Tokyo, Japan)	60 $\times$ universal plan apochromat water-immersion objective, NA 1.2, WD 0.25 mm, correction collar for 0.13- to 0.21-mm coverslips
	PLAPO60XO/TIRFM-2 (Olympus, Tokyo, Japan)	60 $\times$ plan apochromat oil-immersion objective, NA 1.45, WD 0.15 mm. High NA is needed for TIRF microscopy
Dichroic mirrors and interference filters	Z520/10X, Z650/20X (Chroma Technology, Rockingham, Vermont)	Excitation/cleanup filters for 520 and 650 nm, respectively
	Z520RDC-SP-POL, Z650RDC-SP-POL (Chroma Technology, Rockingham, Vermont)	Dichroic mirrors for S and P polarization at 520 and 650 nm, respectively
	3RD560-640 (Omega Optical) XF3083/25 595AF60 (Omega Optical, Brattleboro, Vermont) HQ700/75 (Chroma Technology, Rockingham, Vermont)	Emission filters for 520 nm (Omega) and 650 nm (Chroma) 3RD560-640 (O.D.>8), 595AF60, and HQ700/75 (O.D.>6)
Neutral density filters	NT46-495 (Edmund Optics, Barrington, New Jersey)	Linear ND filter fused silica, 11 steps, 0.04 to 2.0 optical density
Lenses and mirrors	F-LA15 (Newport, Irvine, California)	Diode laser collimating aspherical lens
	COL-UV/VIS-FCPC (Avantes, Broomfield, Colorado)	UV/VIS/NIR collimating lens for optical fiber output with adjustable focus
	KPX021AR.14 KPX058.AR14 (Newport, Irvine, California)	Keplerian beam expander (31.8FL and 88.3FL, respectively)
	KPX112AR.14 (Newport, Irvine, California)	300FL tube lens, focusing emission beam onto the fiber core (acting as confocal pinhole)

**Table 1** (Continued.)

Components	Part Number and Supplier	Description
Optical mounts	34 0523 (Linos Photonics, Milford, Massachusetts)	Oval mirrors to align excitation and emission beams
	065235 065096 (Linos Photonics, Milford, Massachusetts)	Beam deflector cubes c-mount with beam steerer mount
	MT1 ST1XY-D (Thorlabs, Newton, New Jersey)	1/2-in. translation stage, XY translator with differential drives and various posts, post holders
Detectors	Edmund-Optics, Newport (Irvine, California)	Various c-mount tubing, rings, posts, and post holders
	H7422-40P (Hamamatsu, Tokyo, Japan)	Photomultiplier tube 320 to 700-nm wavelength range with quantum efficiency=40% at 580 nm
TCSPC system	SensicamQE (Cooke, Romulus, Midugor)	Peltier-cooled 12-bit digital CCD camera 500 to 3600-s exposure time, readout noise $4\sigma$ -root mean square (rms)
	SPC-630 (Becker & Hickl, Berlin, Germany)	TCSPC card. 7-ps time resolution, 125-ns dead time, enables single-molecule measurements (lifetime/FCS/FCCS) with multidetector operations
	HFAC-26 (Becker & Hickl, Berlin, Germany)	1- $\mu$ A 26-dB TCSPC preamplifier
Microscope stage	HRT-81 (Becker & Hickl, Berlin, Germany)	Eight-channel TCSPC router for PMTs
	NanoView & NanoDrive (Mad City Labs, Madison, Wisconsin)	Manual micrometer two-axis coarse positioning with a piezo-actuated $100 \times 100 \times 100 \mu\text{m}$ 0.2-nm resolution three-axis nanopositioner; NanoDrive interfaces with National Instruments PCI-6071E board
Optical trap	iFLEX 1000 (Point Source, Southampton, United Kingdom)	830-nm cw laser with output power 50 mW
	COL-UV/VIS/NIR-FCPC (Avantes, Broomfield, Colorado)	UV/VIS/NIR collimating lens for optical fiber output with adjustable focus
	LA1422-B LA1608-B (Thorlabs, Newton, New Jersey)	Keplerian beam expander (40FL and 75FL respectively) with IR coating
	675DCSPXR (Omega Optical, Brattleboro, Vermont)	Dichroic mirror $21 \times 33$ mm at 675nm
Computers	PDQDT-10S-SI (Noah, Melbourne, Florida)	Quadrant photodetector module, $1 \times 1$ mm total active area, 350 to 1100-nm spectral range
	Precision 530 (Dell, Round Rock, Texas)	Dual Intel Xeon 2.0-GHz CPU 1-Gbit RAM, hosts National Instruments PCI-6071E & PCI-6711 boards and Cooke board
Chambers and temperature control	Optiplex GX 240 (Dell, Round Rock, Texas)	Intel P4 1.5-GHz CPU 512 Mbits RAM, hosts Becker & Hickl SPC-630 TCSPC board
	FCS2 & controller (Biopetechs, Butler, Pennsylvania)	Focht live-cell chamber system with temperature controller
Optical table	Objective heater and controller (Biopetechs, Butler, Pennsylvania)	Objective heater with temperature controller
	VH36660W-OPT (Newport, Irvine, California)	Research-grade vibration-free optical table

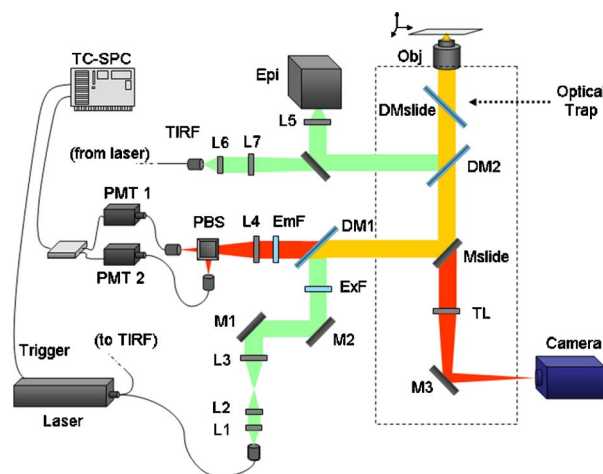


**Fig. 2** Optical setup. The Kr/Ar-ion, diode, or pulsed Nd:YAG laser beam is transmitted via fiber coupling to the TIRF or confocal port. For confocal illumination, upon exiting the fiber, the beam is collimated with lens L1, expanded by lenses L2 and L3, steered by the mirrors M1 and M2, reflected off the dichroic mirror (DM1), and enters the right side port of the microscope (note that the tube lens for the side port has been removed). After excitation of the sample, the fluorescence emission signal is collimated by the objective and exits the side port, passes through the dichroic mirror and is focused—using lens L4—onto the optical fiber which is connected to the photomultiplier tube (PMT). A polarizing beamsplitter (PBS) can be introduced before the fiber to separate light with polarization that is parallel or perpendicular to that of the excitation light. The PMTs convert single photons to electrical pulses, which are routed to the TCSPC board. Laser light from the TIRF system shares the back port of the microscope with the epifluorescence tube (Epi). Lenses L5 and L6 collimate the epifluorescence and TIRF light, respectively. The TIRF illumination is focused at the objective back aperture by the lens L7. When the sliding mirror, Mslide1, is removed from the light path, the right side port is closed and the emission signal can be collected by the camera via the tube lens (TL). In addition, the optical trap can be inserted above the fluorescence cube turret with an infrared dichroic mirror (DMslide) mounted on a custom-built slider (not shown).

ensured by using emission filters with attenuation optical densities (ODs) of 6 or more. High-quality emission filters are necessary to ensure good SNRs in single-molecule experiments.

Collimated fluorescence light is focused with a 250-mm-focal-length lens onto a  $50\ \mu\text{m}$ , 0.22 NA optical fiber, which serves as the confocal pinhole. The optical fiber entrance is mounted on a three-axis manual micrometer stage to optimize the confocal probe volume such that autocorrelation curves are consistent with diffusion models. The fluorescence light emerging from the optical fiber is focused onto a GaAsP photomultiplier tube (PMT) which has high gain and is optimized for single-photon counting for wavelengths of 320 to 700 nm with a peak wavelength of 580 nm. The quantum efficiency of the PMT is 40% at peak wavelength (manufacturer's data) and its response time is  $\sim 8$  ps.

The photon detection event is converted into an electronic pulse, which is routed through an eight-channel router to the TCSPC module for collection and analysis. The TCSPC electronics digitally tag incoming pulses such that the photon arrival time relative to the beginning of the experiment (macro-time) and relative to the laser pulse time (microtime) are

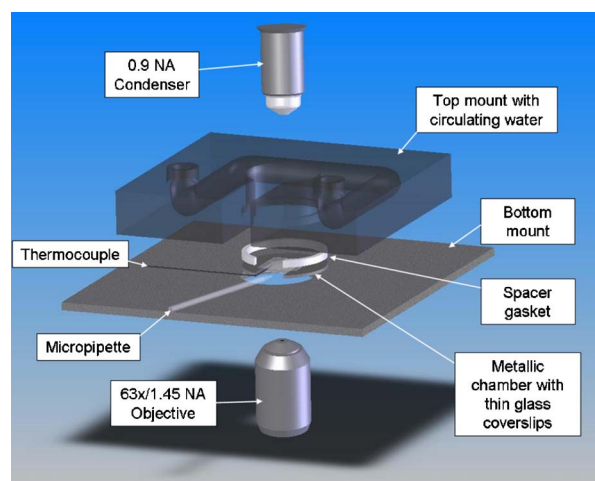


**Fig. 3** Custom micromanipulation chamber comprised of mounting plate, silicone spacers, metallic chamber with a side aperture, thermocouple for temperature monitoring, micropipette for micromanipulation, and the water circulation chamber.

measured. A preamplifier prevents overloading of the PMT by shutting it down in response to high photon counts. The data are continuously written into a FIFO (first in, first out) buffer in the SPC-630 board. For a detailed description of the principles behind TCSPC, see the excellent monograph by Becker.<sup>33</sup>

### 3.5 Optical Trap

The optical trap was first modeled using ray-tracing software (Optics-Lab, Carlsbad, California) to assist in lens placement. The trap was constructed using C-mount components and is introduced into the expanded infinity space under the microscope objective (Fig. 2). Coherent 830-nm laser light can be continuous or transistor-transistor logic (TTL)-modulated using a 5-V square wave with 50% duty cycle from an analog-to-digital (A/D) board (National Instruments, Austin, Texas). A water-immersion  $60\times/1.2$ -NA objective is used to focus the collimated and expanded laser beam down to a diffraction-limited spot. The coordinates of the laser focal point corresponding to the image is determined by imaging the focused beam reflecting off the back of a glass coverslip. Dielectric polystyrene beads in a solution of 1% albumin and DPBS were then successfully trapped and tracked with a spatial sensitivity of  $\sim 10$  nm using time-lapse digital imaging and particle tracking algorithms based on the methods of Gelles et al.<sup>34</sup> TTL-modulation of the laser power enabled precise modulation of trap strength for rapid mechanical testing of 3% gelatin/water solution, which has elastic properties similar to endothelial cell cytoplasm.<sup>35</sup> We recently integrated a quadrant photodiode above the condenser, which will enable 3-D tracking of trapped microbeads and photonic force microscopy.<sup>36</sup>

### 3.6 Chambers for Micromanipulation and Flow

We designed a temperature-controlled micromanipulation chamber (Fig. 3) for TCSPC measurements and imaging of cells and membranes undergoing application of forces with a micropipette or an optical trap. The position of the micropi-

ette inside the chamber is controlled by a motorized, three-axis micromanipulator with a computer interface (MP-285, Sutter Instruments, Novato, California). The micropipette tip is shaped on a microscope-based microforge using a low-melting-temperature glass bead and a micromanipulator.

For microaspiration, raising or lowering an adjustable reservoir relative to a reference reservoir produces an intake or outflow of water at the tip of the micropipette. A variable-pressure transducer (Validyne, Northridge, California) attached to both reservoirs generates a voltage proportional to the relative height difference, which is then converted to a digital signal using an A/D board (National Instruments, Austin, Texas). The transducer system is sensitive to pressure changes of  $\sim 1 \text{ dyn/cm}^2$  ( $\sim 0.001 \text{ cm}$  of water).

Chamber temperature is monitored using a thermocouple and maintained by using circulating water from a temperature-controlled water bath (TC500, Brookfield, Middleboro, Massachusetts). The accuracy and stability of the temperature control in the chamber is  $\pm 0.1^\circ\text{C}$ . For microscopy of live cells under continuous shear flow we use a commercial flow chamber system (FCS2 system, Biopetech, Butler, Pennsylvania). The chamber has a thermistor-based temperature controller and an objective heater to maintain constant temperature. Physiological pH is maintained by perfusing humidified 5%  $\text{CO}_2$  gas and culture media through an oxygenator (Living Systems Inc., Brattleboro, Vermont).

## 4 Materials and Methods

### 4.1 Preparation of Dye Solutions for FCS and Fluorescence Lifetime Measurements

We obtained 9-(2-(ethoxycarbonyl)phenyl)-3,6-bis(ethylamino)-2,7-dimethyl, chloride [rhodamine 6G (R6G)] powder from Invitrogen (Eugene, Oregon) and used it without further purification. The dye solutions were dissolved and diluted in distilled water to a final R6G concentration ranging from 1 to 10 nM. Fresh dye solutions were prepared before the start of each experiment. In experiments designed to demonstrate the relationship between diffusion and solvent viscosity, water-based solutions containing 5 nM of R6G and 10 to 80 % (v/v) of reagent-grade glycerol (Fisher Scientific, Hampton, New Hampshire) were prepared. The bulk viscosities of the prepared solutions were measured using a cone-and-plate viscometer (Haake Rotovisco 1, Thermo Electron, Waltham, Massachusetts). For the simultaneous FCS and lifetime measurements, a pulsed 650-nm red laser was used to excite 1,1'-dioctadecyl-3,3',3'-tetramethylindodicarbocyanine, 4-chlorobenzenesulfonate (DiD, Probes, Eugene, Oregon) in dimethylsulfoxide (DMSO, EMD chemicals, Gibbstown, New Jersey), ethanol, methanol, or dimethyl formamide (DMF) (Sigma-Aldrich, St. Louis, Missouri). Experiments were performed at room temperature unless otherwise specified.

### 4.2 Preparation of Giant Unilamellar Vesicles

Giant unilamellar vesicles were prepared based on the method by Dimitrov and Angelova<sup>37</sup> with minor modifications. 1,2-Dimyristoyl-*sn*-glycero-3-phosphocholine (DMPC) (Avanti polar lipids, Alabaster, Alabama) and 0.001 mol% 1,1'-dioctadecyl-3,3',3'-tetramethylindodicarbocyanine perchlorate (DiI-C<sub>18</sub>) (Invitrogen, Eugene, Oregon) were dis-

solved in chloroform. After vacuum drying this mixture onto nitinol wires, the assembly was placed in a  $55^\circ\text{C}$  chamber containing 0.1-M sucrose and an alternating current was applied across the wire electrodes. A LabView-controlled A/D board (National Instruments, Austin, Texas) was used to apply to the wires 0 to 1 V in increments of 50 mV at 5-min intervals, followed by a constant voltage of 1.2 V for 3 h. The sizes of the resulting giant unilamellar vesicles varied from 10 to 70  $\mu\text{m}$ .

### 4.3 Cell Culture and Staining Protocols

Bovine aortic endothelial cells (BAECs) (VEC Technologies, Rensselaer, New York) were subcultured between passages 3 and 10 in T-25 flasks. Culture medium consisted of MCDB-131 complete medium (450 mL) supplemented with 50 mL FBS (fetal bovine serum), 10 ng/mL EGF (epidermal growth factor), and 1  $\mu\text{g/mL}$  hydrocortisone with addition of 50  $\mu\text{l/mL}$  100 $\times$  antibiotic/antimycotic solution, 90  $\mu\text{g/mL}$  heparin, and 0.2 mg/mL ENDO GRO (VEC Technologies, Rensselaer, New York). Cells were incubated in this medium at  $37^\circ\text{C}$  with 5%  $\text{CO}_2$  and grown to confluence on No. 1 glass coverslips. Cell membranes were stained using DiI-C<sub>18</sub>. The DiI-C<sub>18</sub> stock solution was prepared in DMSO and diluted with phosphate-buffered saline (PBS) (no calcium, magnesium, or albumin) to a final concentration of 1  $\mu\text{M}$  (for imaging) and 1 nM (for FCS measurements). After rinsing the cells three times in PBS without calcium or magnesium, the cells were incubated with the staining solution for 3 to 5 min at  $37^\circ\text{C}$ . The cells were rinsed five times and returned to the PBS with calcium, magnesium, and 1% albumin. The cells were maintained at physiological pH and temperature in the incubators and while conducting the FCS measurements.

### 4.4 Curve Fitting of Autocorrelation and Lifetime Data

Autocorrelation curves were fit with Eqs. (6)–(9) as appropriate, using the Levenberg-Marquardt nonlinear least-squares regression algorithm with the aid of Origin software (Originlab, Northampton, Massachusetts). Quality of fits was assessed by minimizing residuals and  $\chi^2$  values. The structure factor obtained from the fit was between 2 and 6 in all the experiments performed.

For the lifetime measurements, the IRF was collected from a sample of a dilute scattering solution of aqueous dairy creamer colloidal particles using the pulsed red diode laser before the start of each experiment. The full width at half maximum (FWHM) of the IRF when the 650-nm diode laser was at a high power setting was calculated to be  $\sim 300$  picoseconds (see Sec. 5.4). The fluorescence lifetime data of DiD dye in various solvents were collected subsequently. Fluorescence decay curves were extracted from histograms of photon arrival times (relative to laser pulse times) by a process of iterative deconvolution using Eq. (12) in Fluofit software (PicoQuant, Berlin, Germany). Data were fit using a biexponential decay curve with the  $\chi^2$  values of the fit between 1 and 1.5. Using an additional exponential did not result in an improved fit. In some cases, diffusion coefficients and lifetimes are expressed as averages  $\pm$  standard deviation.

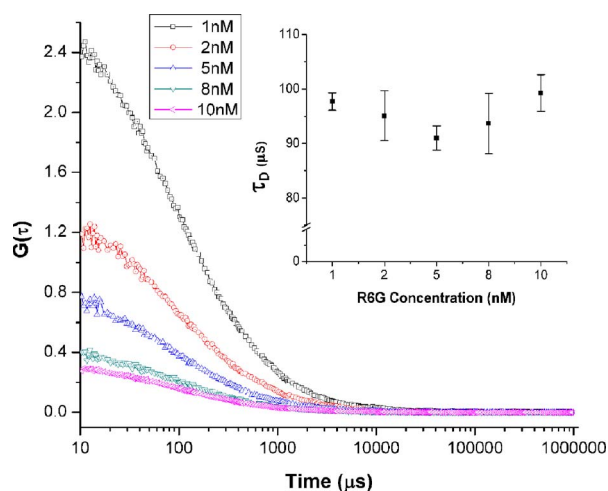


**Fig. 4** Sample autocorrelation curves for various concentrations of rhodamine 6G ranging from 1 to 10 nM;  $G(0)$  (inversely proportional to the average number of particles in the observation volume) was determined by fitting autocorrelation functions with Eq. (6). Inset: The average diffusion times  $\tau_D$  of R6G molecules obtained from fitting autocorrelation curves with Eq. (6) (error bars indicate the standard deviation of 10 measurements).

## 5 Results

### 5.1 Effects of Dye Concentration on FCS-Determined Diffusion Coefficients

Rhodamine 6G (R6G) was used to calibrate FCS because of its known diffusion coefficient ( $2.8 \times 10^{-6} \text{ cm}^2/\text{s}$  in water), high quantum yield ( $\sim 0.95$ ), and the relatively large absorption cross section<sup>38,39</sup> ( $1.7 \times 10^{-16} \text{ cm}^2$  at 514.4 nm). Using these known values for rhodamine dye diffusion, we computed the radius of the focal volume to be  $0.326 \pm 0.010 \mu\text{m}$ . This value compares favorably with the theoretically computed values of the radius of the focal volume of  $0.264 \mu\text{m}$ . This experimental radius of the confocal volume was used in all subsequent experiments on cells and vesicles to compute the respective diffusion coefficients. To test whether dye concentration would affect the resulting diffusion coefficients (for example, due to aggregation), we measured the dye diffusion coefficient at progressively increasing concentrations of R6G of 1, 2, 5, 8, and 10 nM in distilled water at room temperature. For each concentration level, 10 autocorrelation curves were obtained and the resulting diffusion coefficients were averaged (Fig. 4). The value of the autocorrelation curve at  $\tau=0$  s,  $G(0)$ , is inversely proportional to the average number of molecules present in the confocal volume [Eq. (6)]. Values of  $G(0)$  increased from 0.3 to 2.49, corresponding to decreasing average particle concentrations of 3.3 to 0.40, which are consistent with the number of molecules calculated from the known concentration of diffusing dye (data not shown). The values of  $\tau_D$  for the five concentrations of R6G measured was approximately  $95 \mu\text{s}$  (inset of Fig. 4) indicating that diffusion of the R6G dye for very dilute concentrations is independent of the number of molecules in the confocal volume. The effective volume ( $V_{\text{eff}}$ ) of the confocal volume measured in this study can be approximated using<sup>23</sup> the equation  $V_{\text{eff}} = \pi^{3/2} r_0^2 z_0$ , where the radius of the confocal volume  $r_0$  is calibrated from the experiment (326 nm) and  $z_0$  is the value of

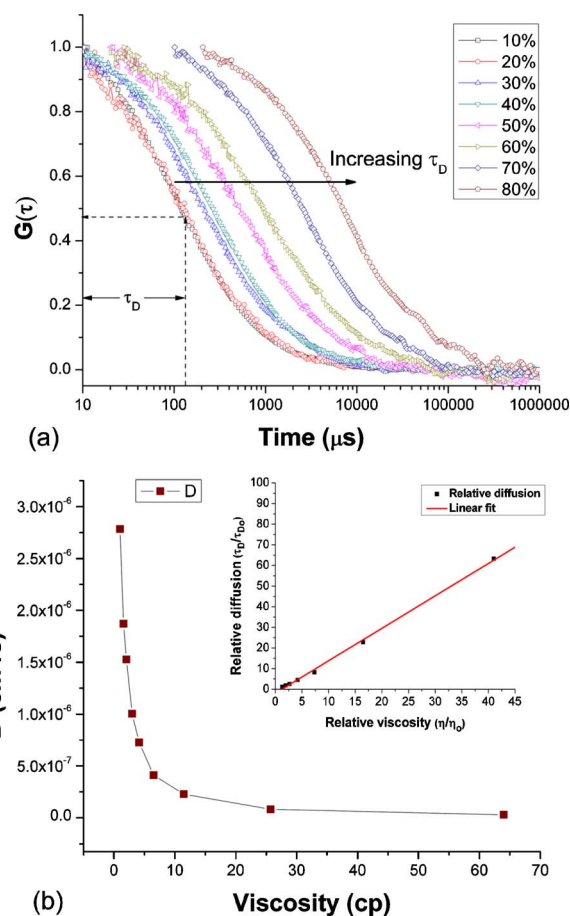


**Fig. 5** (a) Dependence of the autocorrelation curve of R6G on viscosity of glycerol/water solution, where an increase of viscosity (corresponding to increasing percentage of glycerol, v/v) leads to longer characteristic diffusion times  $\tau_D$ , and (b) diffusion coefficients ( $D$ ) of 5-nM R6G obtained by fitting autocorrelation curves in (a) with Eq. (6). The x axis indicates the values of viscosity of the dye solution measured with a cone-and-plate viscometer. Inset figure: The relationship between normalized viscosity ( $\eta/\eta_0$ ) and normalized characteristic diffusion time ( $\tau_D/\tau_{D0}$ ) fit with a line;  $\eta_0$  and  $\tau_{D0}$  are viscosity and characteristic diffusion time, respectively, of dye in pure water.

the axial half-height obtained from the structure factor. The confocal volume of our one-photon FCS setup calculated in this way is  $0.889 \pm 0.09 \text{ fL}$  when averaged over all the 50 measurements of the R6G concentrations. The term “one photon” indicates that fluorescence excitation is accomplished using a one-photon mechanism rather than two photons and that confocality is achieved using a pinhole placed in a conjugate image plane.

### 5.2 Effects of Solvent Viscosity on FCS-Determined Diffusion Coefficients

To assess the sensitivity of FCS-determined diffusion coefficients to solvent viscosity, fluorescence fluctuation analysis was performed on R6G dye dissolved in aqueous solutions of glycerol concentrations ranging from 10 to 80% glycerol. The solution bulk viscosities were measured in a cone-and-plate viscometer. Ten FCS measurements were collected for each solution, autocorrelation curves were computed, and diffusion coefficients were averaged [Fig. 5(a)]. All the experiments

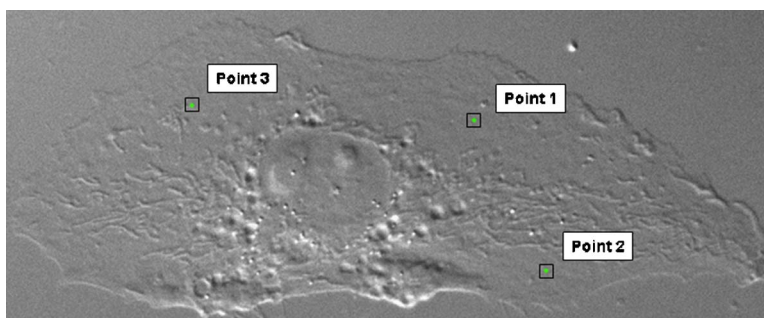


**Fig. 6** Bovine aortic endothelial cell imaged with DIC microscopy. Superimposed points in the image indicate location of confocal volume on the membrane surface of a representative cell from which fluorescence fluctuation data were collected. The cell in this figure corresponds to cell 1 in Table 2.

were performed at room temperature. The average  $\tau_D$  ranged from a value of 0.1 ms for 10% glycerol to 6.5 ms for 80% glycerol. Data in Fig. 5(b) show that FCS-determined diffusion coefficients decrease with increasing viscosity in a manner consistent with Eq. (1). In addition, values of viscosity obtained from FCS-determined diffusion coefficients using Eq. (1) differed from bulk viscosity measurements obtained by cone-and-plate viscometry by 4 to 20%, indicating a good correspondence between the two methods (data not shown).

### 5.3 FCS Measurements of DMPC Giant Unilamellar Vesicles and BAEC Membranes

FCS measurements were performed on DMPC vesicles and endothelial cell membranes stained with DiI-C<sub>18</sub> dye excited with 520-nm light from the cw laser or 532-nm light from the pulsed solid state laser. Fluorescence light with wavelengths of 545 nm and longer was collected for analysis. For cells and vesicles, 5-nM DiI was found to best ensure sufficient fluorescence signal and the ease of fit of autocorrelation curves. About 40,000 photons/s were collected and the number of fluorescent molecules in the probe volume at any time was between 1 and 8. The laser beam position in the  $x$  and  $y$  plane, relative to the imaging system, was assessed by preparing a single monolayer of DiI on a glass coverslip and bleaching it with the laser. The coordinates of the laser spot were then recorded using the camera. During FCS measurements, the position of the focus in the  $z$  axis was adjusted to correspond to the membrane by moving the microscope objective such that fluorescence intensity was maximized.

For DMPC vesicles, 20 FCS measurements were taken at the giant unilamellar vesicle (GUV) apical region, and no more than 5 measurements were obtained on a single vesicle. The temperature in the chamber was maintained at 26°C, which is above the phase-transition temperature (24°C) for DMPC. The results were fit using the equation for 2-D diffusion [Eq. (7)] to obtain a diffusion coefficient for DiI-C<sub>18</sub> in DMPC vesicles of  $5.7 \pm 1.4 \times 10^{-8}$  cm<sup>2</sup>/s.

In BAECs, moving the stage such that the confocal volume intersected the desired location on the membrane apical surface enabled FCS measurements on spatially distinct points on a cell (Fig. 6). FCS measurements were performed on five cells at three points in each cell, and 5 measurements were recorded at each point for a total of 75 measurements. Schwille et al. showed that the diffusion of DiI in a rat baso-

philic leukemia cell membrane can be assessed using models for 2-D, two-species fit or anomalous diffusion.<sup>24</sup> In another recent study, Gielen et al. reported that the diffusion on a nerve cell was well described using a 2-D, two-species fit.<sup>40</sup> Consistent with this finding, we observed that a model for 2-D, two-species diffusion fit the autocorrelation curves better than models for either anomalous subdiffusion or 2-D single species. Thus, Eq. (8) was used to determine diffusion coefficients in BAEC membranes. Values given in Table 2 represent averages of five FCS measurements taken on the cell and point indicated. Analysis of a 2-D, two-species fit gives a fast fraction (considered to be unbound dye) and a slow fraction (which is considered to be the membrane mobile fraction). The proportion of dye in the membrane, therefore, ranged from 78 to 93%, with an average value of 83% and exhibited diffusion coefficients ranging from  $1.75 \pm 0.3 \times 10^{-8}$  to  $7.03 \pm 1.5 \times 10^{-8}$  cm<sup>2</sup>/s. The value of the fast fraction (or unbound dye) ranged from 7 to 22% with an average value of 17% with a diffusion coefficient ranging from  $2.11 \pm 1.1 \times 10^{-6}$  to  $6.27 \pm 3.5 \times 10^{-6}$  cm<sup>2</sup>/s. Two-sample  $t$  test statistics were used to analyze the differences between diffusion coefficients at different points on a given cell with  $p < 0.05$ . As an indication of heterogeneity in diffusion in living cells, statistically significant differences in slow-component diffusion between at least two points on a given cell were found in every cell tested (see Table 2). Representative plots of the autocorrelation function, curve fits, and residuals from cell and model membranes are shown in Fig. 7.

### 5.4 Fluorescence Lifetime Measurements

We measured the fluorescence lifetime of DiD dissolved in the polar protic solvents, ethanol and methanol, and polar aprotic solvents, dimethyl sulfoxide (DMSO) and dimethyl formamide (DMF). In contrast to polar aprotic solvents, polar protic solvents have dissociable H<sup>+</sup> and can form hydrogen bonds. They also have lower dielectric constants and lower dipole moments than polar aprotic solvents. Since fluorescence lifetime depends on the electronic cloud configuration of the dye molecule, these solvents are expected to affect fluorescence lifetime by altering electron distribution and intramolecular charge transfer. In each solvent, fluorescence lifetimes were best fit using biexponential decays [Eq. (12)], consistent with earlier results<sup>41</sup> for DiI. Each value reported in Table 3 represents the average of 10 measurements. Lifetime

**Table 2** Diffusion coefficients of FCS measurements obtained from BAECs.

	Bovine Aortic Endothelial Cells—Diffusion Coefficient Using 2-D, Two Species Fit								
	Point 1			Point 2			Point 3		
	$D_1$ ( $\times 10^{-6}$ cm <sup>2</sup> /s)	$b_2$	$D_2$ ( $\times 10^{-8}$ cm <sup>2</sup> /s)	$D_1$ ( $\times 10^{-6}$ cm <sup>2</sup> /s)	$b_2$	$D_2$ ( $\times 10^{-8}$ cm <sup>2</sup> /s)	$D_1$ ( $\times 10^{-6}$ cm <sup>2</sup> /s)	$b_2$	$D_2$ ( $\times 10^{-8}$ cm <sup>2</sup> /s)
Cell 1	2.58±0.4	0.84±0.01	2.54±0.1	3.01±0.6	0.79±0.79	3.95±0.3 <sup>a</sup>	3.15±1.6	0.82±0.02	2.74±0.7 <sup>b</sup>
Cell 2	2.32±1.1	0.82±0.02	1.75±0.3	4.29±0.9	0.79±0.01	4.50±0.3 <sup>a</sup>	4.13±0.9	0.82±0.02	4.48±1.3 <sup>a</sup>
Cell 3	2.85±1.4	0.82±0.02	3.62±0.3	5.29±2	0.85±0.01	5.20±0.4 <sup>a</sup>	6.27±3.5	0.83±0.01	5.94±0.4 <sup>ab</sup>
Cell 4	2.86±2.7	0.78±0.06	5.17±3.0	4.08±3.3	0.88±0.01	3.99±1.1	4.91±1.1	0.85±0.02	7.03±1.5 <sup>b</sup>
Cell 5	3.58±2.4	0.86±0.01	5.21±1.7	5.47±0.8	0.85±0.01	6.91±0.7	2.11±1.1	0.85±0.03	2.19±0.1 <sup>ab</sup>

2-D, two-species fit was performed on 75 measurements, obtained from five different cells. Three different spatial points were chosen for each individual cell (see Fig. 6). Here,  $D_1$  and  $D_2$  are diffusion coefficients of the fast and slow moving components of Dil molecules, respectively; (not shown)  $1-b_1$  and  $b_2$  are their respective relative fractions.

Two-sample  $t$  test analysis was used to determine whether differences in diffusion coefficients between points were statistically significant.

<sup>a</sup>Significant difference between point 1 and points 2 or 3 ( $p < 0.05$ ).

<sup>b</sup>Significant difference between point 2 and point 3 ( $p < 0.05$ ).

Slow component diffusion values ranged from  $1.75 \times 10^{-8}$  to  $7.03 \times 10^{-8}$  cm<sup>2</sup>/s and averaged  $4.38 \pm 1.62 (\times 10^{-8})$  cm<sup>2</sup>/s [mean  $\pm$  standard deviation (SD)].

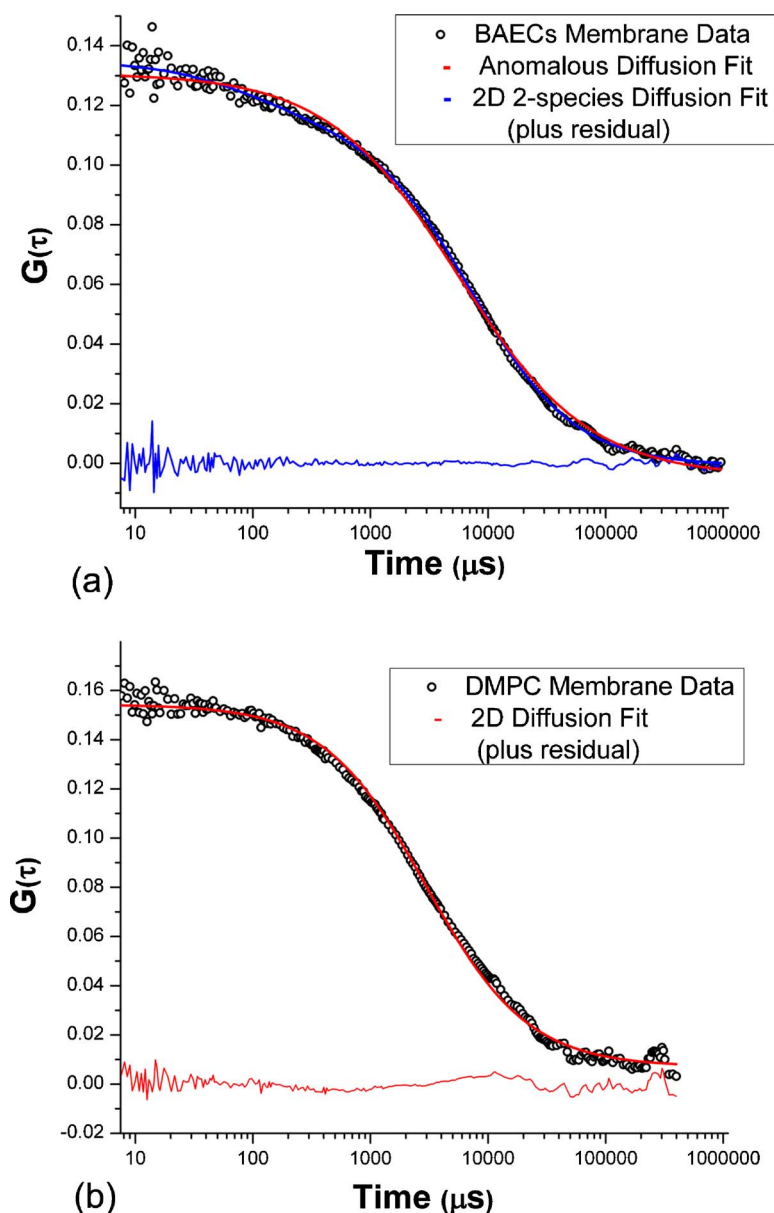


**Fig. 7** (a) Representative plots of the autocorrelation of fluorescence intensity fluctuations arising from BAEC membranes stained with 5-nM DiI-C<sub>18</sub>. Autocorrelation functions were fit with Eqs. (7)–(9) describing 2-D diffusion (one species), 2-D diffusion (two species), and anomalous diffusion, respectively. The residual of the 2-D, two-species fit is shown at the bottom of the graph (blue line). (b) Representative autocorrelation curve and 2-D diffusion fit of DiI-C<sub>18</sub> in a DMPC membrane. The residual of the fit is shown at the bottom of the graph.

values for ethanol and methanol were  $(\tau_1, \tau_2)$  0.48, 1.22 and 0.40, 1.02 ns, respectively, suggesting that fluorescence lifetime can be different even in closely related solvents. Buschmann et al. obtained the fluorescence lifetime values of DiD in various solvents.<sup>42</sup> Using a single exponential to fit the lifetime curve, they obtained a value of 1.12 ns for the decay of DiD in ethanol. In our experiments, the characteristic diffusion times  $\tau_D$  of DiD in DMSO and DMF were 51.2 and 47.8  $\mu$ s, respectively. However, the fluorescence lifetimes of the dye (using a biexponential decay) were 0.74, 1.57 and 1.10, 1.93 ns, in DMSO and DMF, respectively (Table 3). Thus, molecules with similar diffusion characteristics can be readily distinguished based on lifetime. Fluorescence emission of DiD in ethanol and methanol is intrinsically weak and

therefore autocorrelation curves were noisy and could not be fit with models for FCS. A representative curve showing the fluorescence decay with a fit along with the instrument response function is shown in Fig. 8.

### 5.5 Optical Trap Microrheometry

The value of the optical trap's spring constant ( $\sim 11$  pN/ $\mu$ m) was determined from particle trajectories in water and the equipartition theorem using Hooke's law. The spring constant of an optical trap was modulated by a TTL pulse delivered to the laser controller. The result was a trap stiffness exerted on polystyrene beads that varied as a square wave. Bead displacement as a function of time depended on this time-varying trap stiffness and the mechanical properties

**Table 3** Fluorescence lifetimes of DiD in polar protic (ethanol and methanol) and polar aprotic (DMSO and DMF) solvents.

Solvent	Diffusion Time ( $\mu\text{s}$ )	Lifetime (ns) Experiment ( $\tau_1, \tau_2$ )	$\chi^2$	Dielectric Constant <sup>a</sup>	Dipole Moment <sup>a</sup>
Ethanol	NA	0.48, 1.22	1.18	24.3	1.69
Methanol	NA	0.40, 1.02	1.14	33	1.70
DMSO	51.8	1.10, 1.93	1.30	47.2	3.96
DMF	47.2	0.74, 1.57	1.50	38.3	3.82

<sup>a</sup>From the Handbook of Chemistry and Physics tables.

Pulsed laser excitation (650 nm) and TCSPC were used to determine fluorescence lifetime. Photon arrival time histograms were fit with a biexponential decay [Eq. (12)]. Diffusion of DiD in the polar aprotic solvents, DMF and DMSO, was determined using FCS and Eq. (6). Fluorescence emission of DiD in polar protic solvents, ethanol and methanol, was sufficient for lifetime analysis but too weak to generate an autocorrelation curve which could be fit. NA=not applicable.

of the matrix surrounding the bead. To demonstrate the interaction of beads and a viscoelastic environment, a mixture of 3% gelatin and filtered water—intended to mimic the cell cytoplasm—was combined with beads in a solution of 1% albumin and DPBS. Trapped-bead locations were imaged and tracked with custom tracking software. When the trap was turned on, a large time-dependent displacement of the bead toward the center of the trap was observed (Fig. 9). The time-

lag of displacement relative to the laser power indicated that the bead was in a viscoelastic environment. Thus, modulating optical trap forces and measuring the time-dependent displacements of beads provides a convenient means to measure the viscoelastic properties of endothelial cells without moving the cells or the trap location.

### 5.6 Multimodal Microscopy

The optical system permits sequential imaging from DIC, epifluorescence, and TIRF imaging modalities with minimal instrument manipulation. As an example, DIC, epifluorescence, and TIRF images of DiI-C<sub>18</sub>-stained BAECs are shown in Fig. 10. The great majority of the cells were stained on the membrane. The TIRF imaging is sensitive to membrane basal topography in which bright areas correspond to a membrane that is adherent to the cover glass.

## 6 Discussion

The CMDM described in this paper was designed to address the following fundamental issues in mechanotransduction research: (1) forces are spatially distributed; (2) relationships between force application and cell perturbation require the integration of continuum and molecular-scale predictive models; and (3) determination of molecular activation requires temporal and spatial registration of single-molecule events in live, intact cells under controlled conditions. To meet these design criteria, we constructed and calibrated a multimodal microscope for cellular imaging and single-molecule fluores-

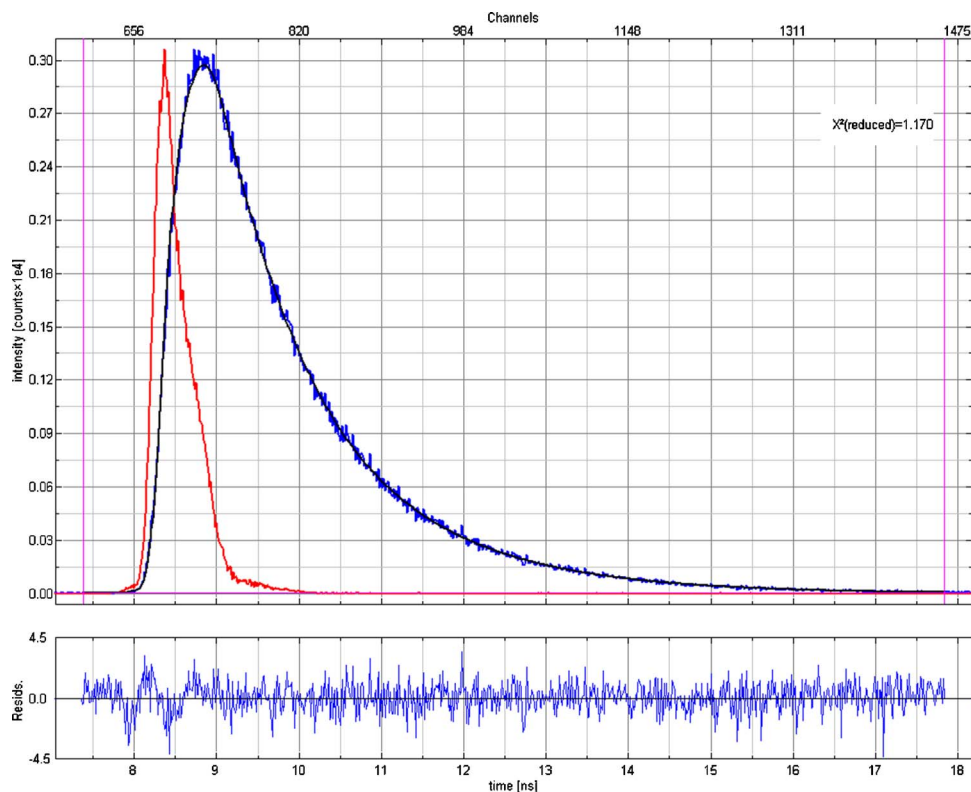


**Fig. 8** Fluorescence decay (blue line) and instrument response function (red line) for DiD fluorescence in ethanol. The decay histogram is fit with a double exponential (black line) to obtain the fluorescence lifetime. The  $\chi^2$  value of the fit is 1.17. The FWHM of the instrument response function is  $\sim 300$  ps.

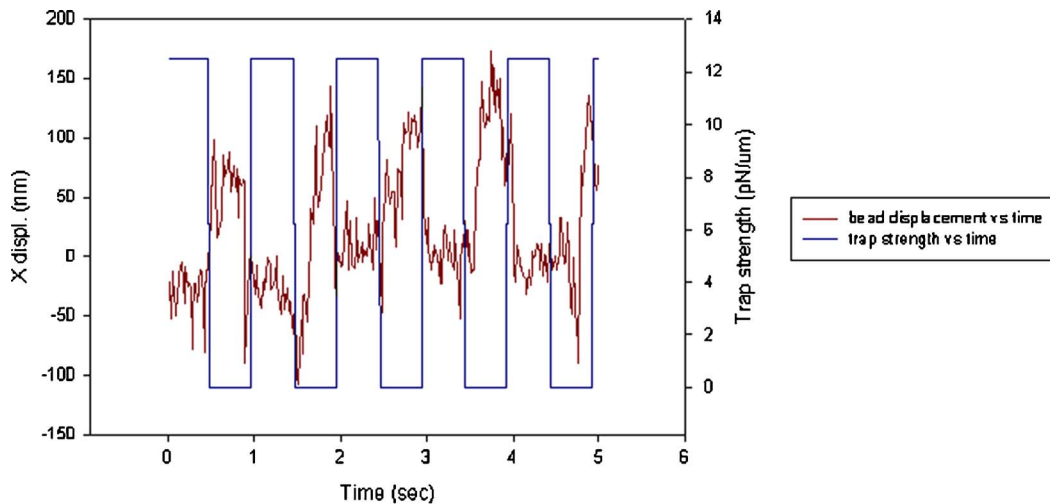


**Fig. 9** TTL trap induced displacement of a 0.5- $\mu\text{m}$  bead embedded in a 3% gelatin solution. The TTL trap can also operate in continuous mode. Trap stiffness was determined to be 11 pN/ $\mu\text{m}$  by tracking thermally induced displacements of trapped 0.5- $\mu\text{m}$  polystyrene beads in DPBS and 1% albumin. The statistical variance of  $x$  coordinates for trapped beads was computed and compared to the potential energy and trap spring constant using Hooke's law and the equipartition theorem. TTL modulation enables analysis of time-dependent responses of the surrounding environment of the bead in response to step changes in trap strength.

cence detection and analysis. First, collection volume of the fluorescence emission was reduced to  $<1$  fL using a fiber aperture placed in a plane confocal to the laser focus. Second, fluorescence was collected with high-detection efficiency PMTs. Third, noise arising from stray laser light, autofluorescence, and fluorescence from glass coverslips and impurities in the solution was systematically reduced or eliminated by using high-quality optical filters. Fourth, all systems (confocal and trap) were spatially correlated to positions on the cell through careful 3-D calibration of the focus point and imaging plane of the multimodal microscope.

### 6.1 Improvements in FCS Instrumentation

In contrast to majority of the more traditional FCS instruments, which use avalanche photodiodes (APDs) for photon detection, we employ single photon counting PMTs. These newer PMTs (e.g., Hamamatsu H7422-40P) have a higher quantum efficiency than older generation PMTs, making them suitable for photon correlation studies.<sup>33</sup> In addition, PMTs are easier to align (because their active area is larger (squared millimeters versus squared micrometers), less susceptible to photon-induced degradation, and have a superior response time (tens of picoseconds) compared to APDs (hundreds of picoseconds). These properties also make them optimal for fluorescence lifetime measurements. Thus, use of PMTs enables fluorescence lifetime and FCS data to be obtained from a single set of measurements.<sup>43</sup>

We use software to generate autocorrelation curves from FIFO data obtained from TCSPC instrumentation (i.e., TCSPC-FCS). Hardware autocorrelator cards can also generate autocorrelation curves in near real time, using current fluctuations from APDs or PMTs. However, when combined with pulsed-laser excitation, TCSPC instrumentation records all photon arrival times and saves them into memory directly. This feature makes all the raw photon data available for additional computational analysis necessary for generation of photon counting histograms (PCHs), multispectral fluores-

cence lifetime imaging (FLIM), burst-induced fluorescence lifetimes (BIFL), and higher order correlations without the necessity for an additional, expensive, hardware correlator.<sup>33,43</sup> Advances in TCSPC instrumentation and modern autocorrelation software algorithms (e.g., the multitau time correlation method) ensure near real time autocorrelation curves that were previously only possible with dedicated hardware correlators.<sup>44</sup> Recent studies support the increasing use of TCSPC for FCS and lifetime measurements.<sup>43</sup>

### 6.2 FCS Can Detect Subtle Changes in Dye Concentrations

To test whether the system could detect subtle changes in concentration of diffusing species, we performed FCS analysis of autocorrelation curves arising from diffusion of rhodamine dye, which varied in concentration from 1 to 10 nM. These calibration experiments support the use of FCS to determine the absolute number of molecules in the observation volume. Absolute molecular concentrations are essential in the study of the binding kinetics of molecules present on the surfaces of cell membranes and in solution.<sup>45</sup> In the context of mechanotransduction, it is thus possible to follow a surface signal transduction pathway by following the association and disassociation of a receptor complex in response to an externally imposed force from fluid flow. One of the main limitations of the technique of FCS is the requirement of extremely low concentrations of probe molecules. We observed degradation of correlation signal with dye concentrations greater than  $10^{-8}$  M. While the requirement for low concentrations of molecules in FCS makes imaging impractical, it is an advantage in studies of binding kinetics in cells, where the concentrations of aggregating molecules are typically low. The low concentration also means the molecular events in cells can be studied with relatively less perturbation of the biological system compared to methods which require high concentrations of fluorescent molecules such as fluorescence

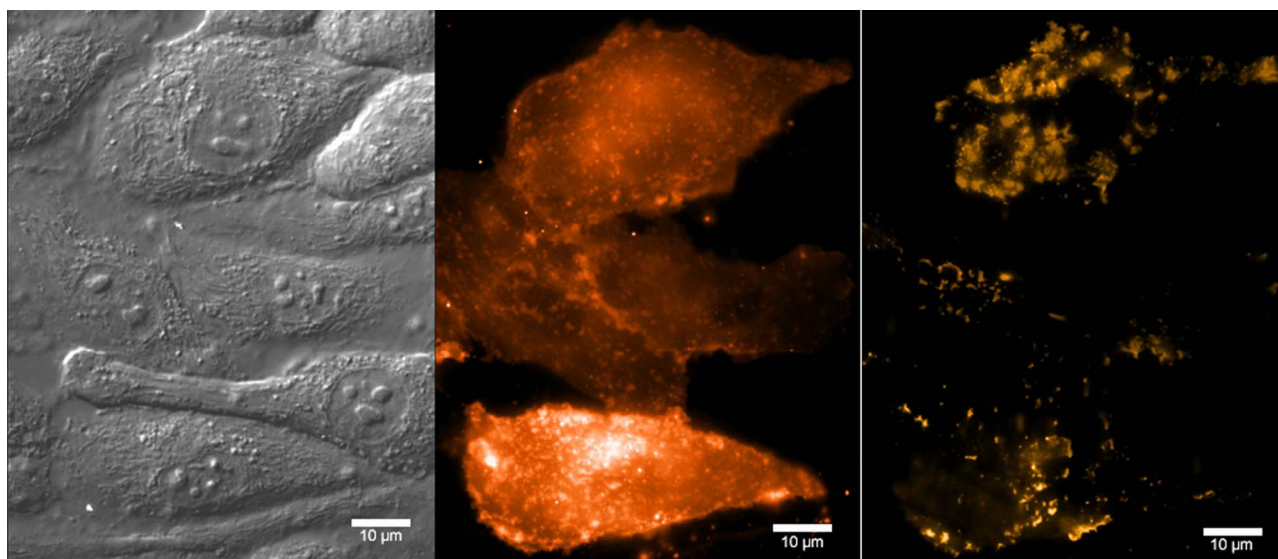


**Fig. 10** Dil- $C_{18}$ -stained bovine aortic endothelial cells imaged sequentially with DIC, epifluorescence, and TIRF.

recovery after photobleaching (FRAP) and any imaging-based methods such as fluorescence resonance energy transfer (FRET).

### 6.3 FCS-Determined Diffusion Coefficients Are Sensitive to Small Changes in Viscosity

In our calibration experiment, we show that increases in glycerol concentration resulted in right-shifted autocorrelation curves indicating longer diffusion times for increasingly viscous environments [Fig. 5(a)]. Thus, FCS is likely to be sufficiently sensitive to monitor subtle changes in the local microviscosity, which may be biologically significant. In our recent study, we showed that the diffusion of DiI in cellular membranes is not uniform and varies substantially in response to applied shear over the cells.<sup>46</sup> Combined with 3-D piezo-scanning, FCS can monitor such changes occurring in cells due to imposed fluid flow or other mechanical perturbations to determine spatially resolved mechanical effects on membranes.

### 6.4 Differences in DiI Diffusion in Cell and Model Membranes Determined by FCS

To test whether the CMDM could detect spatially varying diffusion of lipids in cell and model membranes we measured the fluorescence fluctuations arising from DiI in model DMPC membranes and bovine aortic endothelial cells. Model membranes are useful in studying diffusion in lipid bilayers, phase segregation in lipids, and model protein diffusion in vesicles.<sup>47,48</sup> They are compositionally simple and homogeneous in nature enabling one to fit the simple 2-D equation [Eq. (7)] of diffusion to the autocorrelation curves. In DMPC vesicles above the phase transition temperature, we obtained diffusion coefficient values of  $5.7 \pm 1.4 \times 10^{-8}$  cm<sup>2</sup>/s. More importantly, the small differences of diffusion values obtained within measurements performed on one vesicle and between different individual vesicles support the assumption that the vesicles are homogeneous in nature and that the FCS measurement is repeatable. Almeida et al.<sup>49</sup> and Vaz et al.<sup>50</sup> ob-

tained values of the diffusion coefficients in DMPC/Chol bilayers at various temperatures using FRAP. At 303 K, the value of  $D_L$  for a pure DMPC bilayer was  $\sim 6 \times 10^{-8}$  cm<sup>2</sup>/s, which agrees well with the value obtained in the current study. FRAP experiments in other model membranes of POPC (1-palmitoyl-2-oleoyl-*sn*-glycero-3-phosphocholine) show unrestricted translational diffusion  $D = 4.4 \times 10^{-8}$  cm<sup>2</sup>/s in fluid membrane and restricted diffusion  $D = 0.7 \times 10^{-9}$  cm<sup>2</sup>/s in polymer-stabilized membranes.<sup>51</sup> Previous FCS experiments on DLPC (dilauroyl phosphatidylcholine) revealed<sup>47</sup> a translational diffusion coefficient of  $3 \times 10^{-8}$  cm<sup>2</sup>/s.

FCS analysis of DiI fluorescence from stained endothelial cells leads to two important observations. First, the choice of diffusion models used to fit autocorrelation curves of DiI fluorescence in cell membranes is not straightforward, consistent with observations by others.<sup>24,40</sup> To fit our cell lipid diffusion data, we used models for both 2-D, two-species [Eq. (8)] and anomalous subdiffusion [Eq. (9)]. In general, we found that fitting of autocorrelation curves with a model for 2-D, two-species fit resulted in uncorrelated residuals and smaller  $\chi^2$  values. The spatially heterogeneous nature of the cell membrane necessitates the requirement for a complex fit such as that for the 2-D, two-species fit. In our study, the 2-D, two-species fit reveals the existence of a fast-moving component, whose origin is unclear but may reflect unbound dye, as has been suggested in other studies.<sup>40</sup> It has been speculated that the fast component of the diffusion might arise from the unwashed dye present in the focal volume.<sup>40</sup> Measurements of dye in solution away from the membrane support this hypothesis. However, the relatively high fraction (83%) of the mobile membrane component confirms that FCS is effective in measuring cell membrane lipid diffusion. The results obtained by the 2-D, two-species fit compare favorably with membrane diffusion values in the literature<sup>24,40,46</sup> using either FCS or FRAP.

The second important observation in this study is that translational diffusion coefficients for different measurement points on endothelial cells vary significantly (cells 1 to 5,

Table 2). The values for the membrane diffusion on different points on the cells used in this study ranged from  $1.75 \pm 0.3 \times 10^{-8} \text{ cm}^2/\text{s}$  to  $7.03 \pm 1.5 \times 10^{-8} \text{ cm}^2/\text{s}$ . While all the values for membrane diffusion are within the same order of magnitude, the interpoint variation within a single cell or between individual cells used in this study is not trivial, but represents an example of the heterogeneous nature of the membrane surface. The variability in the values of the diffusion coefficient might arise from the complexity of the cellular membrane such as differences in lipid phase and density, local protein concentration and aggregation,<sup>52</sup> and membrane interaction with the cytoskeleton and glycocalyx.<sup>53</sup> Thus, the ability to obtain FCS data from specific locations is an important step toward assessing the nature of spatial heterogeneity of molecular dynamics in live cells.

### 6.5 Time-Resolved Fluorescence of DiD in Polar Protic and Aprotic Solvents

We used our pulsed, red laser to generate data for fluorescence lifetime and FCS to test the ability of the system to deflect subtle differences in how DiD interacts with its immediate surroundings. The measurement of fluorescence lifetime is independent of dye concentration and is solely determined by changes in the dye's photophysics induced by inter- and intramolecular interactions. Data reported in Table 3 suggest that the same fluorescent molecule, DiD, has longer fluorescence lifetimes in aprotic solvents compared to protic solvents (Table 3). Fluorescence lifetime depends on nonradiative decay mechanisms. Thus, the shorter fluorescence lifetimes in protic solvents may be due to such nonradiative decay mechanisms as hydrogen bonding and intermolecular proton transfer. Newer modalities of FLIM exploit this ultrasensitivity of a fluorophore for changes in its immediate surrounding to generate spatial maps of lifetime.<sup>43</sup> It is expected that lifetime analysis will enable rapid mapping of mechanically induced, molecular-scale perturbation of the dye-lipid-water microenvironments in intact cell membranes.

### 6.6 Optical Trap Microrheometry of Viscoelastic Gelatin Solutions

An additional goal of this project was to integrate a means for mechanical testing and force application on single adherent cells. Thus, we constructed an optical trap which used a simple, well-controlled TTL waveform to modulate the trap stiffness to assess the time-dependent mechanical properties of living cells. A TTL-modulated optical trap was successful in identifying viscous and elastic properties of a gel matrix, but further analysis is required to ensure that polystyrene beads are attached to the gel matrix. Future research will also include the development of a mathematical model of viscoelasticity for a time-dependent spring constant.

## 7 Conclusions

Integrated instrumentation and interdisciplinary approaches will help solve biological and medical problems originating from the interface of cellular signaling and cell mechanics, an emerging area of biology. Finite element modeling, Monte Carlo simulations, and molecular dynamics can provide predictive multiscale models of cell behavior. However, due to the level of complexity involved in the cellular signal trans-

duction and inherent compartmentalization of cellular signaling in microenvironments, verification of models must be done at the single-molecule level on intact cells with high-precision spatial registration. Alterations in the dynamics of molecules are assumed to accompany changes in their signaling (e.g., phosphorylation and dimerization). Such changes are detectable by FCS and fluorescence lifetime analysis, making single-molecule spectroscopy an ideal tool to address the precise molecular mechanism by which forces induce changes in cellular biology.

Some possible future avenues of investigation are monitoring the diffusion-related kinetics of transmembrane proteins such as G-protein-coupled receptors in response to externally applied forces due to fluid flow, micropipette aspiration, or an optical trap. One of the authors (P.J.B.) has performed earlier work<sup>46</sup> showing changes in membrane fluidity in response to shear flow using FRAP. The study can be extended to spatially map the changes occurring on a plasma membrane with single-molecule sensitivity using the current instrumental setup. The current setup can also potentially be used to follow the differential kinetics of protein molecules at the apical and basal surfaces of the cell by combining the techniques of one photon FCS with TIR.

In conclusion, we have successfully built a multimodal microscope that combines microscale monitoring of molecular dynamics at multiple time scales with prescribed macroscale force conditions. This system addresses an unmet need for integration of force application, analysis of cell mechanics, and molecular-scale mechanotransduction detection. It is now possible to forge new research directions in which cell-specific, multicomponent models of mechanotransduction are developed from 3-D live cell imaging and validated with molecular-scale biological readouts.

### Acknowledgments

We would like thank Ahmed Heikal, PhD (Penn State), and Axel Bergman, PhD (Becker-Hickl), for their helpful discussions and trouble-shooting of TCSPC. This work was supported in part by a grant to P.J.B. from the National Heart Lung and Blood Institute (R01 HL 077542-01A1), by a National Science Foundation Career Award to P.J.B. (BES 0238910), and by a seed grant to P.J.B. from the Center for Optical Technologies, Bethlehem, Pennsylvania. R.M. was supported by the Penn State Biomaterials and Bionanotechnology Summer Institute (NIBIB-NSF EEC-0234026).

### References

1. A. W. Orr, B. P. Helmke, B. R. Blackman, and M. A. Schwartz, "Mechanisms of mechanotransduction," *Dev. Cell* **10**, 11–20 (2006).
2. D. E. Ingber, "Mechanobiology and diseases of mechanotransduction," *Ann. Med.* **35**, 564–577 (2003).
3. P. F. Davies, "Overview: temporal and spatial relationships in shear stress-mediated endothelial signalling," *J. Vasc. Res.* **34**, 208–211 (1997).
4. K. A. Barbee, T. Mundel, R. Lal, and P. F. Davies, "Subcellular distribution of shear stress at the surface of flow-aligned and non-aligned endothelial monolayers," *Am. J. Physiol.* **268**, H1765–H1772 (1995).
5. A. B. Mathur, G. A. Truskey, and W. M. Reichert, "Atomic force and total internal reflection fluorescence microscopy for the study of force transmission in endothelial cells," *Biophys. J.* **78**, 1725–1735 (2000).
6. A. Trache and G. A. Meininger, "Atomic force-multi-optical imaging integrated microscope for monitoring molecular dynamics in live

- cells," *J. Biomed. Opt.* **10**, 064023(1–17) (2005).
7. Y. Wang, E. L. Botvinick, Y. Zhao, M. W. Berns, S. Usami, R. Y. Tsien, and S. Chien, "Visualizing the mechanical activation of Src," *Nature (London)* **434**, 1040–1045 (2005).
  8. H. Huang, C. Y. Dong, H. S. Kwon, J. D. Sutin, R. D. Kamm, and P. T. So, "Three-dimensional cellular deformation analysis with a two-photon magnetic manipulator workstation," *Biophys. J.* **82**, 2211–2223 (2002).
  9. G. T. Charras and M. A. Horton, "Determination of cellular strains by combined atomic force microscopy and finite element modeling," *Biophys. J.* **83**, 858–879 (2002).
  10. M. C. Ferko, B. P. Patterson, and P. J. Butler, "High-resolution solid modeling of biological samples imaged with 3-D fluorescence microscopy," *Microsc. Res. Tech.* **69**(8), 648–655 (2006).
  11. E. A. Osborn, A. Rabodzey, C. F. Dewey, Jr., and J. H. Hartwig, "Endothelial actin cytoskeleton remodeling during mechanostimulation with fluid shear stress," *Am. J. Physiol.: Cell Physiol.* **290**, C444–C452 (2006).
  12. C. Sultan, D. Stamenovic, and D. E. Ingber, "A computational tensegrity model predicts dynamic rheological behaviors in living cells," *Ann. Biomed. Eng.* **32**, 520–530 (2004).
  13. N. Wang and Z. Suo, "Long-distance propagation of forces in a cell," *Biochem. Biophys. Res. Commun.* **328**, 1133–1138 (2005).
  14. R. V. Geiger, B. C. Berk, R. W. Alexander, and R. M. Nerem, "Flow-induced calcium transients in single endothelial cells: spatial and temporal analysis," *Am. J. Physiol.* **262**, C1411–C1417 (1992).
  15. I. Levitan, A. E. Christian, T. N. Tulenko, and G. H. Rothblat, "Membrane cholesterol content modulates activation of volume-regulated anion current in bovine endothelial cells," *J. Genet. Physiol.* **115**, 405–416 (2000).
  16. S. Li, M. Kim, Y. L. Hu, S. Jalali, D. D. Schlaepfer, T. Hunter, S. Chien, and J. Y. Shyy, "Fluid shear stress activation of focal adhesion kinase. Linking to mitogen-activated protein kinases," *J. Biol. Chem.* **272**, 30455–30462 (1997).
  17. S. M. McCormick, S. G. Eskin, L. V. McIntire, C. L. Teng, C. M. Lu, C. G. Russell, and K. K. Chittur, "DNA microarray reveals changes in gene expression of shear stressed human umbilical vein endothelial cells," *Proc. Natl. Acad. Sci. U.S.A.* **98**, 8955–8960 (2001).
  18. S. T. Hess, S. Huang, A. A. Heikal, and W. W. Webb, "Biological and chemical applications of fluorescence correlation spectroscopy: a review," *Biochemistry* **41**, 697–705 (2002).
  19. V. Vukojevic, A. Pramanik, T. Yakovleva, R. Rigler, L. Terenius, and G. Bakalkin, "Study of molecular events in cells by fluorescence correlation spectroscopy," *Cell. Mol. Life Sci.* **62**, 535–550 (2005).
  20. E. Haustein and P. Schwille, "Ultrasensitive investigations of biological systems by fluorescence correlation spectroscopy," *Methods* **29**, 153–166 (2003).
  21. E. Elson and D. Magde, "Fluorescence correlation spectroscopy. I. Conceptual basis and theory," *Biopolymers* **13**, 1–27 (1974).
  22. D. Magde, E. Elson, and W. W. Webb, "Fluorescence correlation spectroscopy. II. An experimental realization," *Biopolymers* **13**, 29–61 (1974).
  23. C. Zander, J. Enderlein, and R. A. Keller, *Single-Molecule Detection in Solution Methods and Applications*, Wiley, Berlin (2002).
  24. P. Schwille, J. Korch, and W. W. Webb, "Fluorescence correlation spectroscopy with single-molecule sensitivity on cell and model membranes," *Cytometry* **36**, 176–182 (1999).
  25. J. R. Lakowicz, *Principles of Fluorescence Spectroscopy*, 2nd ed., Springer, New York (1999).
  26. K. C. Neuman and S. M. Block, "Optical trapping," *Rev. Sci. Instrum.* **75**, 2787–2809 (2004).
  27. M. Yanai, J. P. Butler, T. Suzuki, H. Sasaki, and H. Higuchi, "Regional rheological differences in locomoting neutrophils," *Am. J. Physiol.: Cell Physiol.* **287**, C603–C611 (2004).
  28. R. M. Simmons, J. T. Finer, S. Chu, and J. A. Spudich, "Quantitative measurements of force and displacement using an optical trap," *Biophys. J.* **70**, 1813–1822 (1996).
  29. L. A. Hough and H. D. Ou-Yang, "A new probe for mechanical testing of nanostructures in soft materials," *J. Nanopart. Res.* **1**, 495–499 (1999).
  30. W. H. Guilford, D. E. Dupuis, G. Kennedy, J. Wu, J. B. Patlak, and D. M. Warshaw, "Smooth muscle and skeletal muscle myosins produce similar unitary forces and displacements in the laser trap," *Biophys. J.* **72**, 1006–1021 (1997).
  31. M. C. Ferko, M. B. Garcia, and P. J. Butler, "Finite element stress analysis of a multicomponent model of sheared and focally-adhered endothelial cells," *Ann. Biomed. Eng.* **35**, 208–223 (2007).
  32. S. T. Hess and W. W. Webb, "Focal volume optics and experimental artifacts in confocal fluorescence correlation spectroscopy," *Biophys. J.* **83**, 2300–2317 (2002).
  33. W. Becker, *Advanced Time-Correlated Single Photon Counting Techniques*, Springer-Verlag, Berlin (2006).
  34. J. Gelles, B. J. Schnapp, and M. P. Sheetz, "Tracking kinesin-driven movements with nanometre-scale precision," *Nature (London)* **331**, 450–453 (1988).
  35. S. Yamada, D. Wirtz, and S. C. Kuo, "Mechanics of living cells measured by laser tracking microrheology," *Biophys. J.* **78**, 1736–1747 (2000).
  36. A. Pralle, M. Prummer, E. L. Florin, E. H. K. Stelzer, and J. K. H. Horber, "Three-dimensional high-resolution particle tracking for optical tweezers by forward scattered light," *Microsc. Res. Tech.* **44**, 378–386 (1999).
  37. D. S. Dimitrov and M. I. Angelova, "Swelling and electroswelling of lipids—theory and experiment," *Stud. Biophys.* **113**, 15–20 (1986).
  38. J. Widengren, U. Mets, and R. Rigler, "Fluorescence correlation spectroscopy of triplet states in solution: a theoretical and experimental study," *J. Phys. Chem.* **99**, 13368–13379 (1995).
  39. R. F. Kubin and A. N. Fletcher, "Fluorescence quantum yields of some rhodamine dyes," *J. Lumin.* **27**, 455–462 (1982).
  40. E. Gielen, J. Vercammen, J. Sykora, J. Humpolickova, M. Vandeven, A. Benda, N. Hellings, M. Hof, Y. Engelborghs, P. Steels, and M. Ameloot, "Diffusion of sphingomyelin and myelin oligodendrocyte glycoprotein in the membrane of OLN-93 oligodendroglial cells studied by fluorescence correlation spectroscopy," *C. R. Biol.* **328**, 1057–1064 (2005).
  41. B. S. Packard and D. E. Wolf, "Fluorescence lifetimes of carbocyanine lipid analogues in phospholipid bilayers," *Biochemistry* **24**, 5176–5181 (1985).
  42. V. Buschmann, K. D. Weston, and M. Sauer, "Spectroscopic study and evaluation of red-absorbing fluorescent dyes," *Bioconjugate Chem.* **14**, 195–204 (2003).
  43. W. Becker, A. Bergmann, E. Haustein, Z. Petrasek, P. Schwille, C. Biskup, L. Kelbauskas, K. Benndorf, N. Klockner, T. Anhut, I. Riemann, and K. Konig, "Fluorescence lifetime images and correlation spectra obtained by multidimensional time-correlated single photon counting," *Microsc. Res. Tech.* **69**, 186–195 (2006).
  44. M. Wahl, I. Gregor, M. Patting, and J. Enderlein, "Fast calculation of fluorescence correlation data with asynchronous time-correlated single-photon counting," *Opt. Express* **11**, 3583–3591 (2003).
  45. A. Pramanik and R. Rigler, "Ligand-receptor interactions in the membrane of cultured cells monitored by fluorescence correlation spectroscopy," *Biol. Chem.* **382**, 371–378 (2001).
  46. P. J. Butler, G. Norwich, S. Weinbaum, and S. Chien, "Shear stress induces a time- and position-dependent increase in endothelial cell membrane fluidity," *Am. J. Physiol.: Cell Physiol.* **280**, C962–C969 (2001).
  47. J. Korch, P. Schwille, W. W. Webb, and G. W. Feigenson, "Characterization of lipid bilayer phases by confocal microscopy and fluorescence correlation spectroscopy," *Proc. Natl. Acad. Sci. U.S.A.* **96**, 8461–8466 (1999).
  48. K. Bacia, D. Scherfeld, N. Kahya, and P. Schwille, "Fluorescence correlation spectroscopy relates rafts in model and native membranes," *Biophys. J.* **87**, 1034–1043 (2004).
  49. P. F. Almeida, W. L. Vaz, and T. E. Thompson, "Lateral diffusion in the liquid phases of dimyristoylphosphatidylcholine/cholesterol lipid bilayers: a free volume analysis," *Biochemistry* **31**, 6739–6747 (1992).
  50. W. L. C. Vaz, R. M. Clegg, and D. Hallmann, "Translational diffusion of lipids in liquid-crystalline phase phosphatidylcholine multibilayers—a comparison of experiment with theory," *Biochemistry* **24**, 781–786 (1985).
  51. G. J. Schutz, H. Schindler, and T. Schmidt, "Single-molecule microscopy on model membranes reveals anomalous diffusion," *Biophys. J.* **73**, 1073–1080 (1997).
  52. A. Kusumi and K. Suzuki, "Toward understanding the dynamics of membrane-raft-based molecular interactions," *Biochim. Biophys. Acta* **1746**, 234–251 (2005).
  53. J. M. Tarbell and M. Y. Pahakis, "Mechanotransduction and the glycocalyx," *J. Intern. Med.* **259**, 339–350 (2006).